White Rose Research Online

eprints@whiterose.ac.uk
https://eprints.whiterose.ac.uk
Universities of Leeds, Sheffield and York

Deposited via The University of Sheffield.

White Rose Research Online URL for this paper:
https://eprints.whiterose.ac.uk/id/eprint/169908/

Version: Accepted Version

Article:
Sundeep, S., Wang, J.B., Griffo, A. et al. (2021) Anti-resonance phenomenon and peak voltage stress within PWM inverter fed stator winding. IEEE Transactions on Industrial Electronics, 68 (12). pp. 11826-11836. ISSN: 0278-0046

https://doi.org/10.1109/tie.2020.3048286

© 2021 IEEE. Personal use of this material is permitted. Permission from IEEE must be obtained for all other users, including reprinting/ republishing this material for advertising or promotional purposes, creating new collective works for resale or redistribution to servers or lists, or reuse of any copyrighted components of this work in other works. Reproduced in accordance with the publisher's self-archiving policy.

Reuse
Items deposited in White Rose Research Online are protected by copyright, with all rights reserved unless indicated otherwise. They may be downloaded and/or printed for private study, or other acts as permitted by national copyright laws. The publisher or other rights holders may allow further reproduction and re-use of the full text version. This is indicated by the licence information on the White Rose Research Online record for the item.

Takedown
If you consider content in White Rose Research Online to be in breach of UK law, please notify us by emailing eprints@whiterose.ac.uk including the URL of the record and the reason for the withdrawal request.

UNIVERSITY OF LEEDS
University of Sheffield
UNIVERSITY of York

Anti-resonance Phenomenon and Peak Voltage Stress within PWM Inverter Fed Stator Winding

Shubham Sundeep, Jiabin Wang, *Senior Member, IEEE,* Antonio Griffo, *Member, IEEE,* and Fernando Alvarez-Gonzalez.

***Abstract*—The high-frequency behavior of the stator winding is synthesized herein using a multi-conductor transmission line model to study the potential location of excessive voltage stress, being the main cause of insulation failure within the winding. The comprehensive modeling approach proclaims that the voltage distribution within the winding is a result of the anti-resonance phenomenon, which can be characterized by two oscillatory responses. One of the oscillatory response may lead to excessive voltage stress at the terminals of the machine, which have been reported extensively. However, it is the other oscillatory response, which engenders maximum voltage stress at the neutral end to the winding and prevails due to the superposition of traveling voltage waves. The latter is a sole characteristic of the stator winding and may be more detrimental to the winding insulation. Therefore, the stator winding remains under stress even with short or no cable. Furthermore, the paper illustrates that increasing the cable up to a certain length can be potentially treacherous. The simulation results validate the identified phenomenon through the high-frequency model of the cable and the stator winding developed in MATLAB/Simulink environment. Further, the experimental results verify the aforementioned phenomenon on an automotive-grade 60 kW permanent magnet synchronous machine (PMSM).**

***Index Terms*— Anti-Resonance Frequency, Cable Effect, Common Mode Impedance, Differential Mode Impedance, Multi-Conductor Transmission Line Model, Non-Linear Voltage Distribution, Reflected Wave Phenomenon.**

I. INTRODUCTION

Recent advances in the development of wide bandgap (WBG) devices and embedded control electronics have enabled their applications in a wide range of electric drives for improved efficiency and power density. High switching frequency and low losses offered by WBG devices are particularly attractive in the operation and control of high-speed drives, and high power low inductance motors, which requires pulse train of high switching frequency and fast slew rates and have high bandwidth current regulation strategy to maintain current harmonics within acceptable limits [1-2].

However, a high-frequency (HF) pulse train with a fast slew rate impinging at the terminals of the machine gives rise to several problems such as transient overvoltage at the machine terminals, HF common-mode (CM) current via cable return path, cable loading due to HF current through parasitic capacitance of the cable, HF current through parasitic capacitance of bearing, and electromagnetic interference (EMI)[3-5]. The transient overvoltage poses a detrimental effect on insulation integrity and the HF currents may lead to premature failure of the bearings and radiation of electromagnetic noise.

When a long cable is employed between the Pulse Width Modulation (PWM) inverter and the machine, transient voltage oscillations occur at the machine terminals contributing overvoltage, which may arise to twice of DC-link voltage [3]. However, insulation failure due to short cable length lacks understanding. In [6], the study shows that the short cable may lead to insulation failure due to the interaction between the anti-resonance frequency of the cable and the second anti-resonance frequency of the winding. However, the experimental evidence shown in this paper suggests that it is the first anti-resonance frequency of the winding, which is potentially treacherous.

Furthermore, enormous efforts [7-18] have reported that the PWM voltage with a high slew rate leads to uneven distribution of voltage within the winding. These efforts have employed a HF model of the stator winding to understand the voltage distribution. The studies illustrate that the voltage distributes non-linearly within the winding, with peak voltage stress across the turns of the line end coil. However, excessive overvoltage in the turns close to the neutral point has not been recognized. This knowledge gap owes to two reasons: (1) inappropriate model representing the stator winding; (2) the voltage distribution being studied under a single voltage pulse in isolation.

Many papers in literature [7-18] have availed the multi-conductor transmission line (MCTL) model to predict the voltage distribution, however, they represented the HF behavior of the winding partially. Adjaey *et.al.* [7] have used coil as an elemental section and represented only the first 4 coils as a cell

Shubham Sundeep, Jiabin Wang, Antonio Griffo, and Fernando Alvarez-Gonzalez are with The Department of Electronics and Electrical Engineering, The University of Sheffield, Sheffield, S1 3JD UK (e-mail: ssundeep1@sheffield.ac.uk; j.b.wang@sheffield.ac.uk; a.griffo@sheffield.ac.uk; f.alvarezgonzalez@sheffield.ac.uk). This work was supported by Engineering and Physical Sciences Research Council-EPSRC Grant EP/S00081X/1.

while the remaining 20 coils were lumped together in one cell. For predicting the voltage stress in each turn, they assumed uniform voltage distribution within the coil. In [11], only the line end coil is modeled, whereas, in [9-10] first two coils are modeled as MCTL and a resistance terminates the second coil. M. T. Wright *et.al* [9] have illustrated that, for accurate prediction of the voltage within the line end coil, two coils are sufficient. They concluded that the effect of adding more number of coils into the model on the voltage distribution within the line end coil diminishes as the number of coils is increased. In [9-10], authors have studied only the line end coil and showed that terminating the line end coil either with the second coil or with a 100 Ω resistance, doesn't affect the voltage distribution in the line end coil. In [11-12], only the first five turns are represented as a transmission line Γ-cell and the model is terminated using a lumped π-cell. However, in [13], studies show that terminating the model with an impedance leads to inaccurate voltage distribution, and therefore, they extended the model for the whole phase. For the accurate prediction of voltage distribution, an appropriate representation of wave reflection and propagation phenomenon within the winding is required. Hence, in [14], the whole winding is represented as a MCTL model.

In the foregoing literature [7-13], the core is assumed as a flux barrier which allows pretermitting the eddy current loss. However, at HF, when the skin depth is less than the laminate thickness, the flux produced by the winding penetrates partially within the iron core and induces eddy current. Therefore, the eddy current loss is incorporated and modelled as a resistance across a Γ-cell in [14]. However, the mutual magnetic coupling between the turns is neglected. To improve model accuracy, this paper follows the modelling process proposed in [15], which employs a current controlled voltage source to account for the mutual coupling.

Nevertheless, available literature [7-18] supports that the series of interconnected Γ- cells are a reasonable model to predict the voltage distribution within the winding if the space variation of the wavelength of the highest frequency component in the voltage pulse is negligible within the length of each cell representing the elemental section of the winding. However, all of them have examined the model with a single voltage pulse in isolation, which leads to the conclusion that the peak voltage stress occurs at the first few turns of the line end coil.

No work, to the best knowledge of the authors, have considered the voltage distribution due to the superposition of transients elicited from the PWM voltage pulses impinging at all three phases. As a consequence, a new approach is required which predicts the voltage distribution under PWM voltage excitation at all three-phase terminals.

In this study, the MCTL model of the stator winding uses certain aspects of the previous work [15] to predict the voltage distribution within the winding. Different from the state-of-art literature [7-18], the results shows that the turns close to the neutral point may also be highly stressed due to the anti-resonance phenomenon of stator windings. The key contributions of this paper are as follows.

1) The voltage stress within the winding is characterized by two oscillatory responses. The relatively HF oscillation reported widely in the literature is restricted to the line end coil. In addition, a relatively low frequency (LF) oscillation of CM nature occurs within the stator winding, causing peak voltage stress at the coils close to the neutral point.
2) Unlike literature [7-18], the study shows that the voltage stress within the winding results from the superposition of voltage transients in all three phases. It is therefore important that all three phases are represented over a PWM cycle in simulations.
3) It is shown that the voltage oscillations at the machine anti-resonant frequency causing excessive voltage stress is a sole characteristic of the stator winding and the winding remains under high voltage stress even with short or no cable.

The rest of the paper is organized as follows. Section-II provides a background of the wave propagation/reflection phenomenon and anti-resonance phenomenon in the cable. In section-III, the MCTL model of the stator winding and cable is explained briefly and section-IV illustrates the location of peak voltage stress and explains it using the theory of traveling waves with the simulation results. In section-V, experimental evidences are presented to support the proposed phenomenon. Section-VI presents the discussion on the interaction between the anti-resonance frequency of the cable and the winding and section-VII gives the concluding remarks.

II. BACKGROUND

A. Wave Propagation and Reflection Phenomenon

The PWM voltage pulses traveling through the cable behaves similar to the transverse electromagnetic (TEM) waves traveling through the transmission lines. Due to wave propagation through the cable and reflection at the machine terminals, the terminal voltage oscillates, whose frequency of oscillation depends on the propagation delay (t_p) as [19],

$$f = \frac{1}{4t_p} = \frac{1}{4l_c\sqrt{LC}} \tag{1}$$

where, l_c is the length of the cable, and L and C are inductance and capacitance per unit length of the cable. As an example, for a two-wire lossless cable of length 1m, inductance $L = 10$ μH/m, and $C = 10$ nF/m, the frequency of oscillation at the open load terminal is 790.56 kHz.

B. Anti-Resonance Phenomenon

In electrical circuits, an anti-resonance is a phenomenon where the amplitude of the response of the circuit is at pronounced minima, and the corresponding frequency is called

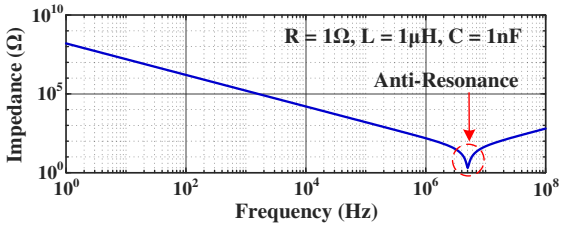

Fig. 1 Frequency response of a series RLC circuit representing anti-resonance behavior.

as anti-resonance frequency. For instance, the impedance of a series RLC circuit is minimum at the frequency $f = 1/2\pi\sqrt{LC}$. This frequency is known as anti-resonance frequency, which is shown in Fig. 1.

The transmission line behavior of a cable can be represented by a series of connected lumped parameter Γ- cells [20] with frequency-dependent parameters to represent the propagation and reflection phenomenon within the cable. Hence, the lumped parameter model of the cable, represented as an electrical circuit, inherits the anti-resonance behavior.

For the cable stated previously, if it is represented using one Γ-cell, the anti-resonance behavior occurs at the frequency (f),

$$f = \frac{1}{2\pi\sqrt{LC}} = 503.29\ kHz \tag{2}$$

At the anti-resonance, the cable model offers the lowest impedance of Z_{min}, but the voltage across the capacitor reaches its maximum of $V/(\omega C \cdot Z_{min})$ for a given excitation voltage of V. Thus, the load terminal voltage oscillates at this frequency. However, this representation does not have sufficient accuracy and hence the anti-resonance frequency differs from the actual frequency of oscillation ($1/4t_p$ = 790.56 kHz). When the same cable is represented using 2 Γ- cells, the parameter of each cell will be half of the single cell model, and the model can be simplified as an equivalent series LC circuit with frequency-dependent C' as,

$$C' = \frac{L_2 - \dfrac{2}{\omega^2 C_2}}{\dfrac{L_2}{C_2} - \dfrac{1}{\omega^2 C_2^{\,2}}} \tag{3}$$

where L_2 and C_2 represent the parameter of each cell. Thus, the anti-resonance frequency increases to,

$$f = \frac{1}{2\pi\sqrt{LC'}} = 622.18\ kHz \tag{4}$$

In a similar way, as the number of the Γ- cells increases, the cable model represents wave propagation and reflection phenomenon accurately, and its anti-resonance frequency tends towards $1/4t_p$, as inferred from Fig. 2.

For an accurate representation of the propagation and reflection phenomena, the space variation of the shortest wavelength of TEM wave within the length of the cable represented as a single Γ- cell must be negligible. However, using a large number of Γ- cells requires computational resources. Therefore, without loss accuracy, in the following study, the cable and the stator winding are represented with a sufficient number of Γ- cells such that it is acceptable to assume that the anti-resonance frequency is equal to $1/4t_p$.

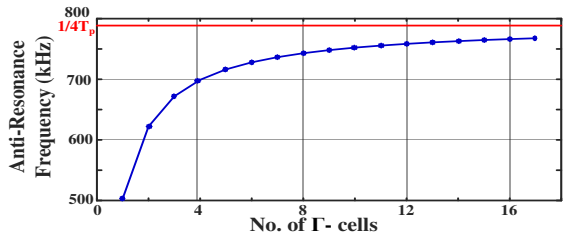

Fig. 2 Anti-Resonance frequency of the cable with different number of Γ-cells.

III. Multi-Conductor Transmission Line Model of Machine Winding

In order to represent the HF behavior of machine windings under PWM voltage excitation, sufficiently high frequency components need to be accounted for. The spectrum of the PWM voltage pulse with amplitude V, switching frequency f_s, rise time t_r, fall time t_f, spreads up to the frequency f_c [21], where f_c is given by,

$$f_c = \frac{1}{\pi \min\left(t_r, t_f\right)} \tag{5}$$

For a SiC MOSFET based inverter with a typical rise time and fall time of 20 ns, the spectrum spreads up to 15.91 MHz. Therefore, there must be a model, which emulates the behavior of the stator winding until 15.91 MHz. This can be meticulously realized by the MCTL model of the stator winding. As discussed in section-II, the selection for the length of the winding represented by a single transmission cell depends on the tradeoff between the accuracy and the computational burden. Thus, to keep the model less complex without losing accuracy, the PWM voltage spectrum until 3 times f_c is accounted for. Therefore, the shortest wavelength of the PWM voltage in the account is,

$$\lambda_{min} = \frac{\vartheta}{3 f_c} \tag{6}$$

where ϑ is the velocity of the wave inside the winding, which depends on the permittivity of the insulation and the equivalent permeability of winding in a slot. Generally, this velocity is at least a quarter of the speed of the TEM wave in a vacuum, which equals to 75 m/μs [14]. Hence, for a voltage pulse rise time and fall time equal to 20 ns, λ_{min} = 1.57 m. Herein, the analysis is made with 60 kW PMSM used in Toyota Pruis [22], whose stator stack length is 50.8 mm. Henceforth, representing each turn of length 101.6 mm as a Γ-cell renders a less complex model within acceptable accuracy.

A. MCTL Model of Stator Winding

The literature [7-18] shows that in the HF range corresponding to the short rise and fall time of the PWM pulse, the HF eddy current induced in the rotor core confines the flux within the air gap region. Also, the steel laminates act as a flux barrier and confine the flux produced by the winding within the slot, thereby, the single-slot model is sufficient to develop the HF model. In [15], the MCTL model is explained in detail, and the modeling process, herein, is adapted from that study. As mentioned above, each cell of the model illustrated in Fig. 3, represents one turn, and includes the following parameters:

1) Turn self-inductance (L_{ii}) and resistance (R_{ii}) represents the inductance and resistance of turn i. It largely depends on the frequency due to skin and proximity effects.
2) Turn mutual inductance (L_{ik}) and resistance (R_{ik}) represents the mutual magnetic and resistive coupling between turns i and k of the same coil. Akin to the self-inductance, this parameter is also frequency-dependent.
3) Turn-to-core capacitance (C_{i0}) and turn-to-turn capacitance (C_{ik}) represents the electrostatic coupling between turn i and the core and between turns i and k. These parameters are independent of frequency and are calculated using

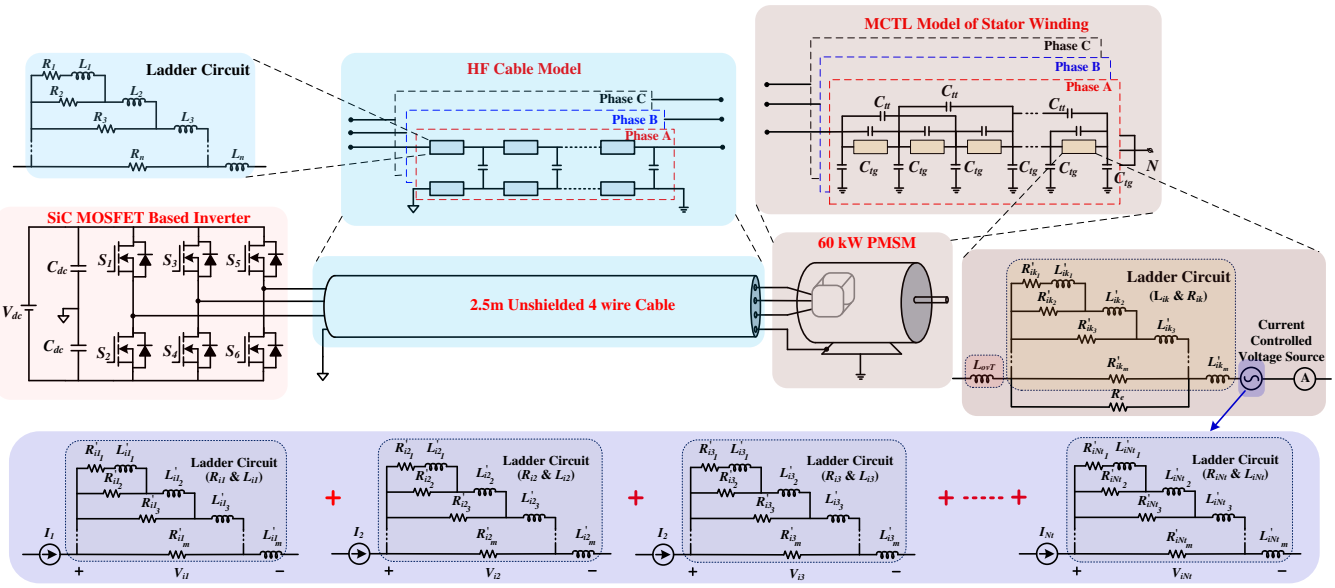

Fig. 3 Simulation configuration for the MCTL model of the stator winding fed by a SiC MOSFET based inverter through the high-frequency model of the cable.

finite element analysis (FEA).

4) Overhang inductance (L_{ovT}) represents the inductance of the turn in the overhang region. For the machine under study, the overhang inductance per turn is 2.8 μH.
5) R_e represents the core loss in the machine due to the penetration of flux in the core. At HF, when the skin depth is comparable to the thickness of the laminates (t), the induced eddy current restricts the flux within the penetration depth (δ) and incurs losses. They are represented as resistance R_e across the ladder network of each turn [15].
6) R'_{ik_n} & L'_{ik_n}, (n = 1,2, …, m) represents the parameters of the m^{th} order ladder network [15] used to model the frequency-dependent R_{ik} & L_{ik}.

B. Parameter Calculation of Transmission Line Cell

Based on the slot parameters [22] outlined in the appendix, a slot model is developed in ANSYS. Further, the resistances (R_{ii}, R_{ik}), inductances (L_{ii}, L_{ik}), and capacitances (C_{ii}, C_{ik}) used in the HF model are calculated using FEA. ANSYS Electrostatic Solver is used to calculate the capacitance (C_{ii}, C_{ik}), whereas, ANSYS Electromagnetic Field Solver is used to calculate the resistances (R_{ii}, R_{ik}) and inductances (L_{ii}, L_{ik}). Without compromising with the accuracy, herein, the variation of dielectric loss due to frequency is neglected.

Due to the skin and proximity effect, the resistance and the inductance representing a turn in the HF model are frequency dependent. To account for the frequency-dependent variation in time-domain analysis, a 5th order ladder circuit [15] is used. The calculation of the parameters of the ladder circuit is explained in [15]. As the turns of the coil are closely packed within the slot, mutual magnetic and resistive coupling exist between the turn conductors of the same coil. However, mutual coupling between the two coils is neglected because of two reasons: (1) The machine understudy has single-layer winding. (2) Due to induced eddy current in the core, no flux originating from two different slots link each other. Therefore, only the mutual couplings between the turns of the same coil is considered. The voltage drop across the turn due to the mutual coupling between the turns of the same coil are expressed mathematically as,

$$V_i = \left(R_{ii} I_i + L_{ii} \frac{dI_i}{dt} \right) + \sum_{\substack{i=1 \\ i \neq k}}^{N_t} \left(R_{ik} I_k + L_{ik} \frac{dI_k}{dt} \right) \qquad (7)$$

where, V_i is the voltage drop across the turn i due to current I_i flowing through it and I_k flowing through k^{th} turn. The second term in (7) accounts for the voltage drop across the turn due to mutual coupling between the turns i and k. Further, the voltage drop across the turn i due to k^{th} turn current I_k is calculated as the voltage drop across the ladder circuit representing the frequency-dependent mutual coupling (L_{ik} and R_{ik}) between turn i and k. Thereafter, a current controlled voltage source is used to account for the voltage drop across each ladder circuit which represents the mutual coupling between the turn i and other remaining turns. This voltage source is connected in series with the ladder circuit representing the self-impedance (R_{ii} and L_{ii}) of turn i, as shown in Fig. 3.

The overhang inductance of the winding is assumed constant and calculated as,

$$L_{ovT} \cong k_r \cdot \frac{1}{N} \cdot \left(\mu_0 N^2 \cdot \left(\frac{2}{P} \right) \cdot \lambda_b \cdot l_{ov} \right) \qquad (8)$$

where, P denotes pole-pairs, N is the number of turn per phase, λ_b is geometry coefficient, l_{ov} is the length of the turn in the overhang region and k_r = 0.3 represents the reduction in the induction of eddy current due to skin effect. Due to the high permeability of the iron core, the flux linking the turns within the stator slot is relatively strong. Therefore, an increase in the resistance of the turns within the slot is significantly higher as compared to the increase in resistance in the overhang region, thereby, the resistance of the overhang region is neglected.

C. HF Model of Cable

Herein, a 2.5 m long, 4 wire shielded cable is used. Akin to the stator winding, the modeling technique and process is also applicable to the cable except that the mutual coupling between

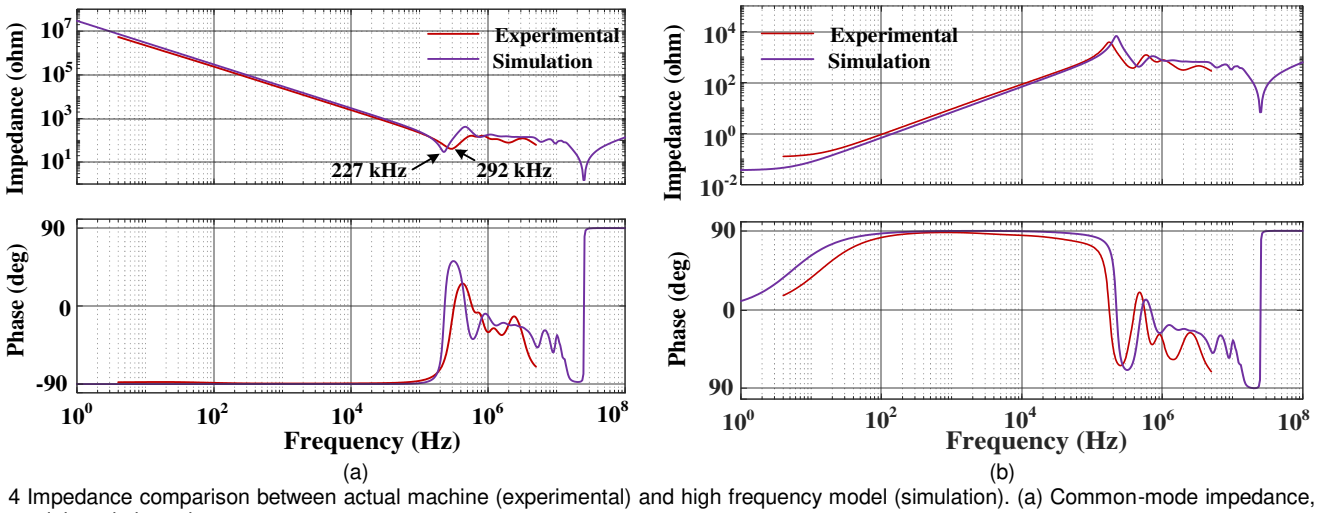

Fig. 4 Impedance comparison between actual machine (experimental) and high frequency model (simulation). (a) Common-mode impedance, (b) Differential-mode impedance.

Γ- cells do not exist. Therefore, only one ladder circuit is used for each cell, which reduces the complexity of the model. To render a less complex model within acceptable accuracy, each cell of the model represents 10 cm length of the cable. Similar to the stator winding model, the capacitive coupling between the phases is assumed to be frequency independent. The MCTL model of stator winding fed by SiC MOSFET based inverter through the HF model of the cable is illustrated in Fig. 3.

IV. Peak Voltage Stress within Stator Winding

A. CM and Differential Mode (DM) Impedances

With the developed model, the CM and DM impedances of the 3-phase stator winding are calculated within a frequency range from 1 Hz to 100 MHz. Meanwhile, the impedance of the actual machine is measured using the HIOKI IM3570 impedance analyzer within its full range from 4 Hz to 5 MHz. The calculated and measured impedances are compared in Fig. 4, where a good agreement between the prediction and measurement is seen albeit some differences exist.

The contrariety between the measured and the calculated results are attributable to the uncertainty and the limitation of the model. Accurate representation of the winding HF behavior requires an infinite number of Γ- cells, which leads to the excessive computational burden. Thus, discretization of the stator winding into a finite number of cells will inevitably introduce errors, particularly in the HF region. Further, the overhang inductance and the core loss resistance are derived from the empirically defined mathematical equation and the curve. In addition, the relative position of turns within a slot in a mush winding is unknown, and differs from the layout assumed in the model, which consequently affects the magnetic and electrostatic coupling between the turns. Moreover, the material properties and the dimensions could differ slightly in the model from the actual winding. However, the key characteristics of both the CM and DM impedances are captured by the model, which enables the prediction of the voltage stress within the winding.

B. Anti-Resonance Phenomenon within Stator Winding

Fig. 4-a indicates the anti-resonance behavior at two different frequencies in the CM impedance of the stator winding, one at

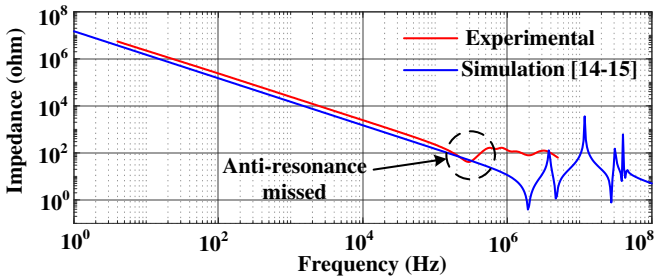

Fig. 5 Comparison between the CM impedance of the stator winding derived from experimental measurement and simulation.

227 kHz, and the other at 25 MHz. Certainly, modeling of each turn as a Γ- cell enables the full representation of the turn-to-core capacitance, thereby, allowing accurate representation of anti-resonance behavior. In [11-12] only the first five turns are modeled as a Γ- cell with remaining turns as single lumped π – cell. Consequently, the CM impedance of the model misrepresents the anti-resonance behavior. Fractional representation of coil-to-core capacitance and inappropriate depiction of wave propagation and reflection phenomenon by representing a large section of winding as a single lumped π – cell leads to misrepresentation of anti-resonance behavior. This is made clear in Fig. 5, which compares the CM impedance of the MCTL model derived from 11-12] and the experimentally measured impedance. The anti-resonance behavior of the stator winding is misrepresented at 2 MHz.

Apart from the CM impedance, from Fig. 4-b, the DM impedance shows a resonance behavior at 200 kHz and an anti-resonance behavior at 25 MHz. The inclusion of skin and proximity effect using a ladder network helped in outlining the resonance frequency clearly.

The CM impedances of the cable and stator winding models under study are illustrated in Fig. 6. It is worth noting that they are of similar characteristics. Both depict the anti-resonance behavior. The stator winding shows the first anti-resonance at a low frequency of 227 kHz as compared to the second one at 25 MHz, whereas, the cable shows multiple anti-resonance starting from 20 MHz. Noteworthy, the combined cable and stator winding CM impedance shows two anti-resonance, one aligns with the 1st anti-resonance of the stator winding and the other

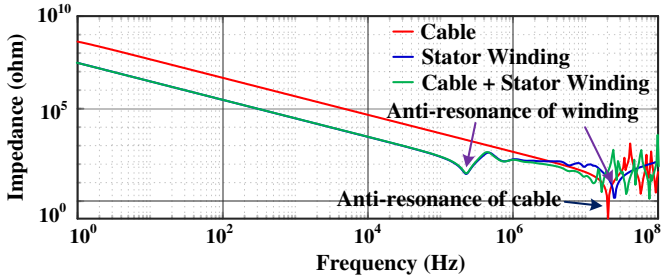

Fig. 6 CM impedance comparison between the cable and the stator winding.

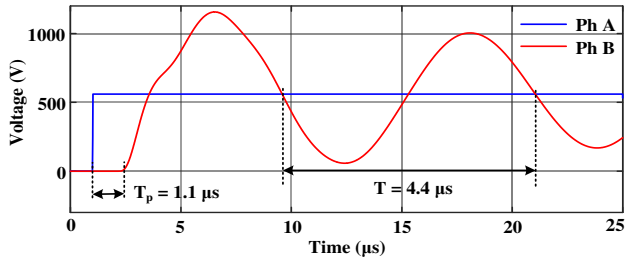

Fig. 7 Incident and reflected voltage wave at phase A and B terminals respectively.

exists close to the anti-resonance of the cable.

C. Wave Propagation and Reflection Phenomenon in Stator Winding

To study the influence of the PWM voltage pulse on the voltage distribution within the winding, the MCTL model of the stator winding developed in MATLAB/Simulink is fed by an ideal inverter model. On exciting phase A with a 560V and 20 ns rise time voltage source, keeping the other two phases floating, the voltage wave propagates from phase A terminal and reaches the phase B terminal after a time delay (T_p), as shown in Fig. 7. Furthermore, phase B terminal voltage oscillates at 227 kHz, which corresponds to the first anti-resonance frequency of the stator winding.

Akin to the cable, the propagation delay is a function of the length of the winding and the wave velocity traveling within it, and is a quarter of the time period of the wave oscillation. Under PWM voltage excitation, the cable and the stator winding offer minimum impedance at their respective anti-resonance frequency, thereby, enduring voltage oscillations.

Due to the high permeability of the core, the anti-resonance occurs in the winding at a much lower frequency. Hence, the frequency of voltage oscillation within the winding is low as compared to the cable. Therefore, hereinafter, the voltage oscillations at the second anti-resonance frequency of the combined cable and stator winding impedance are termed as HF oscillation and the voltage oscillations at the first anti-resonance frequency of the stator winding are termed as LF oscillation.

D. Voltage Distribution under PWM Voltage Excitation

Fig. 8 illustrates the voltage stress between the coils and the core when a PWM voltage pulses at 0.1 modulation index and 40 kHz switching frequency impinge the 3-phase machine terminals. The rise time of the voltage pulse is 20 ns and the DC link voltage is 560 V.

One phase winding of the machine under study consists of 8

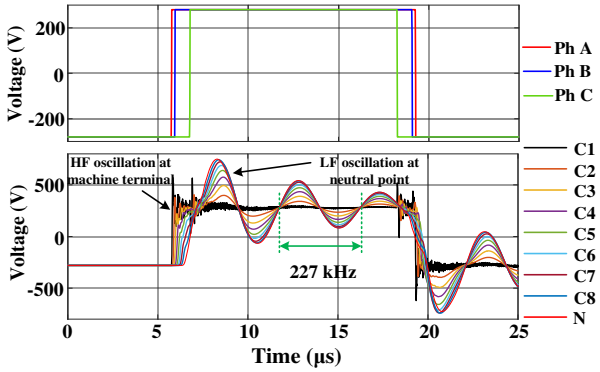

Fig. 8 Inverter output voltage, Coil-to-core, and Neutral-to-core voltage of the stator winding.

series connected coils and each coil has 11 turns. The voltages are measured between the start of the coil and the core (local ground). The principle characteristics in the voltage stress are:

1) The coil-to-core voltage is characterized by two oscillatory responses. This occurs because; the cable and the stator winding endure voltage oscillations at their respective anti-resonance frequency. The LF voltage oscillations correspond to the first anti-resonance frequency of the stator winding and the HF oscillations correspond to the combined second anti-resonance frequency of the cable and stator winding.
2) The HF voltage oscillations are restricted only to the first coil. This is because at this frequency, the shunt admittance of the line end coil offers a low impedance path to the HF current and the series impedance restricts its penetration deep into the rest of the coils.
3) The peak voltage stress occurs due to standing wave oscillating at the first anti-resonance frequency of the stator winding.
4) The peak voltage stress occurs across the neutral and the coils close to the neutral point are most stressed.

A PWM voltage wave impinging on the machine terminal is a spectrum of waves spread over a wide range of frequencies. Consider a voltage component of amplitude V_m and frequency ω impinging phase A terminal at time τ_A, and travel towards phase B. Then, the traveling wave can be mathematically expressed as,

$$v_A(x,t) = V_m \sin\left(\omega\left(t-\tau_A\right)-\frac{\omega x}{\vartheta}\right) \tag{9}$$

where, ϑ is the velocity of propagation of wave within a winding, x represents the position of a turn with respect to phase A terminal, and t represents time. Similarly, another voltage wave of the same magnitude V_m and frequency ω impinging at phase B terminal at time τ_B, travel towards phase A. Then, the traveling wave can be mathematically expressed as,

$$v_B(x,t) = V_m \sin\left(\omega\left(t-\tau_B\right)-\frac{\omega\left(l-x\right)}{\vartheta}\right) \tag{10}$$

Thus, the voltage stress across turn (v_x) in the winding is the superposition of the two traveling waves which is expressed as,

$$v_x(x,t) = 2V_m \cos\left(0.5\omega\tau_{Dwell}+\frac{\omega\left(0.5l-x\right)}{\vartheta}\right)\sin\left(\omega\left(t-0.5\tau_k\right)-\frac{\omega l}{2\vartheta}\right) \tag{11}$$

where, $\tau_{Dwell} = (\tau_B - \tau_A)$ is dwell time, and $\tau_k = (\tau_B + \tau_A)$. This equation can be interpreted as a standing wave with fixed nodes and antinodes. Thus, the superposition of waves of equal magnitude and frequency, traveling in the opposite direction results in a standing wave. Therefore, when the PWM voltage wave impinges the phase terminals, the voltage wave traveling in phase A superposes with the waves traveling in the opposite direction from phase B and C and leads to a standing wave, which oscillates at angular frequency ω. Due to anti-resonance behavior, the winding endures oscillations at the anti-resonance frequency, consequently, the standing waves oscillating at this frequency are more pronounced.

Evidently, from (11), the magnitude of the voltage oscillation depends on dwell time, and is more pronounced if it is short. During the PWM operation of the inverter, the dwell time largely depends on the modulation index and the switching frequency. Under fixed switching frequency and small modulation index, the dwell time is short, consequently, the LF voltage oscillations are more prominent. In addition, the presence of the CM voltage component close to the 1st anti-resonance frequency of the stator winding intensifies voltage oscillation. As an illustration, when the stator winding is excited by PWM voltage switching at 75 kHz, whose third harmonic component is close to the 1st anti-resonance frequency of the stator winding, the magnitude of the LF voltage oscillations plunges to 8 times the 3rd harmonic of the PWM voltage, as shown in Fig. 9. The common mode voltage in the inverter output excites the resonant mode of the machine winding. Thus, if any harmonic component of the switching frequency is brought closer to the anti-resonance of the winding, the peak oscillations is likely to be higher while an opposite trend is true if the harmonic component is far away. Since the peak voltage oscillation at the machine terminals is well-understood, mitigation and quality control measures are currently in place to minimize its effect. In contrast, the peak voltage oscillation close to the star neutral has not been well reported and understood, and no measure currently in place to address this problem. It is from this perspective that the resonance associated with the machine anti-resonance is potentially more harmful, particularly if the switching frequency approaches the machine anti-resonance frequency.

The LF oscillations have not been understood and addressed yet in the literature [7-18] owing to two reasons, (1) use of inappropriate models representing stator winding and, (2) the voltage stress being studied with a single voltage pulse in solitary. Many works of literature [8] have modeled only the line end coil as a MCTL. In addition, they assumed the core as

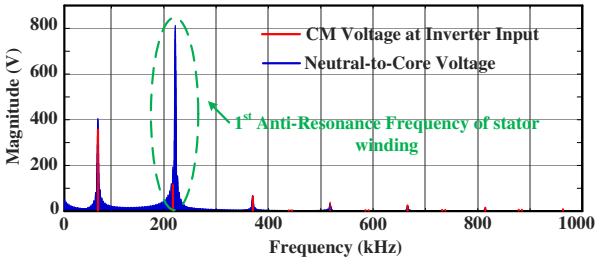

Fig. 9 Comparison of the frequency component of CM voltage at inverter input and Neutral-to-Core Voltage at 75 kHz switching frequency.

an impenetrable sheet and ignored the core loss. Furthermore, in [11-12] only the first five turns are modeled as Γ- cell and the rest are represented as a single π – cell. In [18], although all the turns are represented as Γ- cell, only single-phase is studied in isolation with the application of a voltage front.

The aforementioned methods fail to represent the wave propagation and reflection phenomenon correctly, consequently, fails to represent the first anti-resonance frequency of the stator winding. As shown in Fig. 5, when only the first five turns are modeled as Γ- cell, the first anti-resonance frequency of the model occurs at 2 MHz, which leads to HF oscillations restricted within line end coil, thereby, the work only reported the HF oscillation. In addition, the application of a single voltage pulse in isolation leads to traveling waves and consequently, does not results to voltage stress across the coils close to the neutral point. In [18], authors have shown oscillations in floating phase terminal B and C, when phase A is excited by a voltage pulse. A similar observation can be made from Fig. 7. The floating phases reflect the incident traveling wave (9), wherein, the reflected wave (v_r) is expressed as,

$$v_r(x,t) = V_m \sin\left(\omega\left(t-\tau_A\right) - \frac{\omega(2l-x)}{\vartheta}\right) \tag{12}$$

where, l is twice the length of the phase winding. Thus, the voltage stress (v_x) across the turn located at a distance x from the phase A terminal is the superposition of incident and reflected wave and expressed as,

$$v_x(x,t) = 2V_m \cos\left(\frac{\omega(l-x)}{\vartheta}\right)\sin\left(\omega\left(t-\tau_A\right) - \frac{\omega l}{\vartheta}\right) \tag{13}$$

Thus, the superposition of incident and reflected wave creates a standing wave, which oscillates at angular frequency ω. Due to the anti-resonance behavior, the standing waves oscillating at anti-resonance frequency is more pronounced. It is important to emphasize that, the LF oscillations causing voltage stress near the neutral point are due to anti-resonance behavior, which is the sole characteristic of the stator winding, and will be present even with short or no cables. Thus, irrespective of the winding connection, or the cable length, or any other stator winding configuration, the neutral point voltage oscillates at anti-resonance frequency. However, the configuration only decides the frequency and the damping of the oscillations.

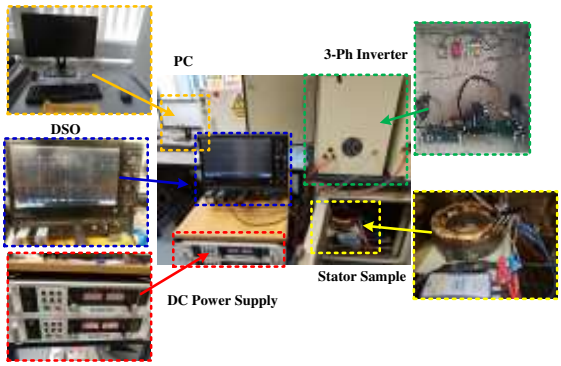

Fig. 10 Experimental rig illustrating Toyota manufactured stator sample fed by 3-phase MOSFET based inverter through 2.5 m shielded cable.

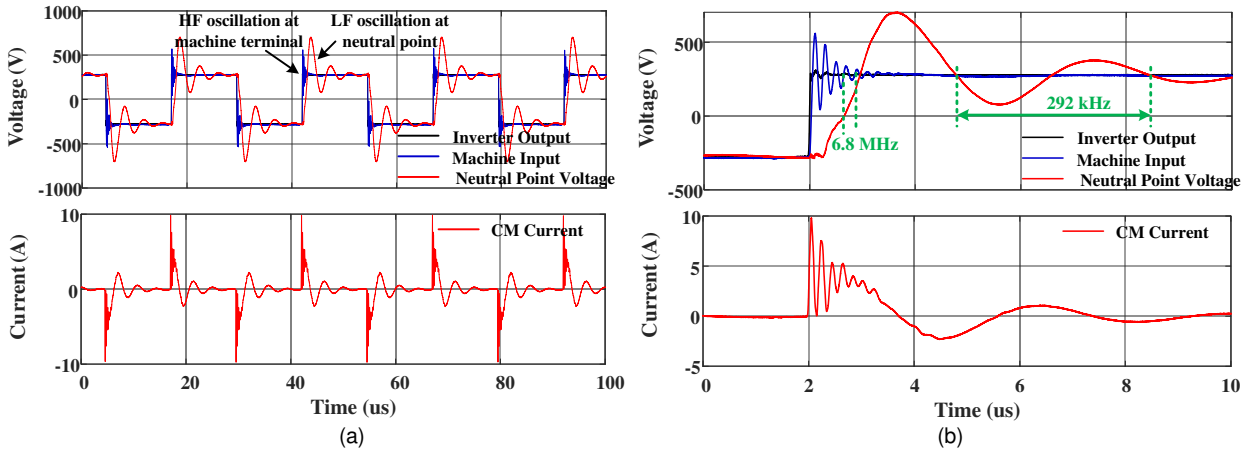

Fig. 11 (a) Inverter output voltage, stator winding terminal voltage, neutral point voltage, and CM current measured during the experiment, (b) during pulse rise.

V. Experimental Validation

For the experimental validation of the proposed phenomenon, a SiC MOSFET based inverter through a 2.5 m cable feeds the 3-phase, 8-pole, 60 kW PMSM under study. The slot dimension and the key features of the machine are outlined in the appendix and described in [22]. During the experiments, the DC link voltage is fixed at 550 V, and the PWM pulse rise time is 20 ns. The switching frequency of the inverter is 40 kHz. As, at HF, the flux is confined in the semi-closed slot region, thereby, no flux links the rotor. Henceforth, the rotor is removed and the experiments are performed on the stator winding at a low modulation index with 0.5 A peak fundamental current. The experimental rig used in this study is illustrated in Fig. 10.

As only the three-phase terminals and the neutral point are accessible, the terminal voltage and the neutral point voltage are measured with respect to the core. Fig. 11 shows the inverter. output voltage measured w.r.t. the mid-point of DC link, motor terminal voltage, and the neutral point voltage w.r.t to the core. Fig. 10 also shows the current flowing through the ground conductor of the cable, known as CM current, measured at the machine terminal. The voltages are measured using a Teledyne Lecroy manufactured 1400V, 100 MHz BW ADP305 high voltage active differential probes, and the current is measured using a Teledyne Lecroy manufactured CP030 30A, 50 MHz BW current probe.

From Fig. 11, the voltage distribution can be characterized by two oscillatory responses. Similar to the simulation results, the HF voltage oscillation is only confined to the terminal voltage and the neutral point voltage oscillates at the first anti-resonance frequency of the stator winding CM impedance. The figure affirms the prediction that the peak voltage stress in this machine occurs at the neutral point. Thus, the experimental results validate the anti-resonant phenomenon of the stator winding under PWM excitation, which persists with short or no cable. It is also noteworthy that, the current through the ground conductor is 90^0 ahead of the voltage, which confirms the capacitive coupling between the winding and the core.

As a difference from the simulation result, the anti-resonance frequency of the winding during experimental validation is 292 kHz, over 227 kHz in simulation (For illustration, see Fig. 4 (a)). Therefore, the voltage stress at the neutral point oscillates at 292 kHz during experiments (Fig. 11 (b)) and at 227 kHz during the simulation (Fig. 8). The difference occurs due to the assumption of the distributed impedance of the winding as a lumped parameter. Also, the randomness in the relative position of turns within the slot and small variation in the material properties and the dimensions causes differences. Howsoever, the key characteristics of the CM impedance, i.e. the anti-resonance, is captured successfully.

VI. Interaction Between the Anti-Resonance Frequency of the Cable and Stator Winding

From the experimental results, it is evident that, at the anti-resonance, the TEM wave endures less damping and hence voltage oscillations sustain for a long period. Therefore, the coil-to-core voltage of the stator winding can be characterized by two oscillatory responses, which depend on the anti-resonance frequencies of the stator winding and cable.

Considering the anti-resonance characteristics, if the anti-resonance frequency of the cable aligns with the first anti-resonance frequency of the stator winding, the voltage wave emerging from the inverter will encounter low damping throughout the cable as well as stator winding and consequently oscillate on a single frequency. Thus, by increasing the cable length to 163 m, the anti-resonance frequency of the cable is reduced to 292 kHz. Under this condition, the voltage wave encounters low damping within the cable and winding, and cause massive coil-to-core voltage stress. This is explicitly illustrated in the following discussion, where the peak-to-peak voltage stress at the neutral point measured with respect to the core is compared with three different cable lengths.

Fig. 12-a illustrates the CM impedance of a 2.5 m long cable with anti-resonance at 19.04 MHz, a 163 m long cable with anti-resonance aligning with the anti-resonance of the stator winding (292 kHz), and a 180 m long cable whose anti-resonance frequency (264 kHz) is lower than that of the stator winding. The combined CM impedance of the cable and the stator winding is shown in Fig. 12-b, wherein, with 2.5 m long cable, the anti-resonance primarily occur at two different frequencies. The LF oscillation at the neutral point occurs due to anti-resonance at 292 kHz (f_{ar1}) and the HF oscillation at the terminal of the machine oscillates at 2nd anti-resonance frequency (f_{ar2}) which occur at 6.8 MHz, as elucidated in Fig. 12-b. However,

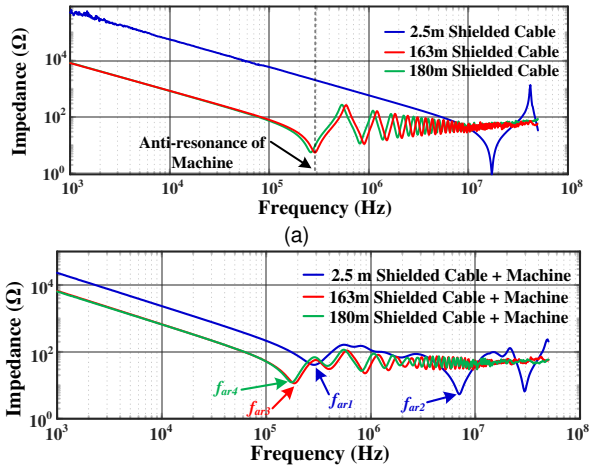

Fig. 12 Comparison of CM impedance measured experimentally with different lengths of cable; (a) CM impedance of the cable, (b) CM impedance of cable connected to the stator winding.

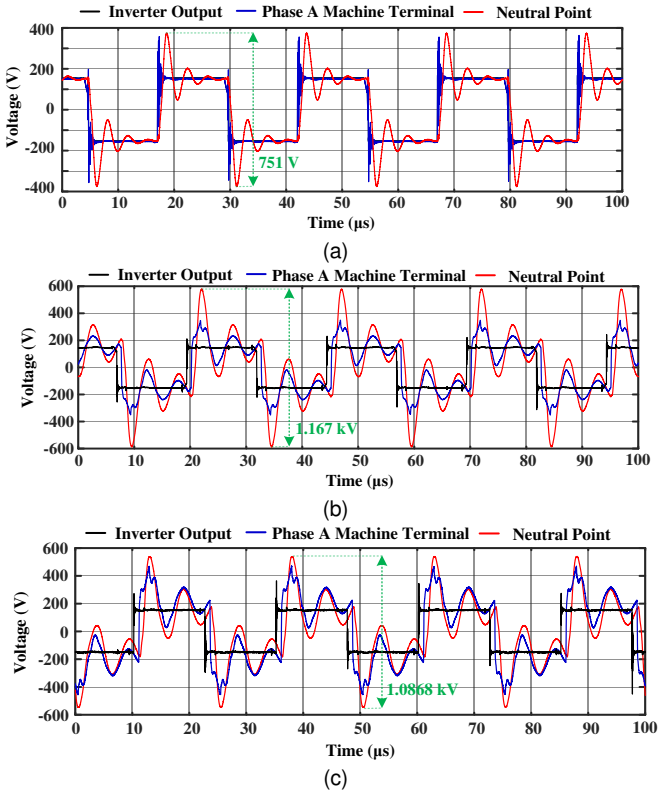

Fig. 13 Experimentally measured voltage stress at the terminal and at the neutral point of the machine with respect to the core (DC Link voltage = 300 V); (a) when the cable length is 2.5 m, (b) when the cable length is 163 m, (c) when the cable length is 180 m.

with 163 m and 180 m long cable, primarily single anti-resonance frequency (f_{ar3} and f_{ar4}) dominates, thereby, the machine terminal and the neutral point voltage oscillate at the same frequency. Due to minimum impedance at f_{ar3} (amongst f_{ar1}, f_{ar3}, and f_{ar4}), the TEM wave traveling within 163 m long cable connected winding, undergo minimum damping, resulting in maximum voltage stress at the neutral point. Therefore, the peak-peak voltage stress at the neutral point when the stator winding is excited with a VSI with 300 V DC link voltage, as illustrated in Fig. 13, is 1.167 kV as compared to 751 V for 2.5 m cable and 1.0868 kV for 180 m cable. Thus, in the worst case scenario, where the cable anti-resonance frequency aligns with that of the stator winding, the groundwall insulation close to the neutral point undergoes maximum voltage stress (3.9 times DC link voltage). Therefore, to avoid any premature failure of the insulation, the anti-resonance frequency of the cable must not be near the first anti-resonance frequency of the stator winding.

VII. Conclusion

Based on the analysis, it has been proclaimed that the voltage distribution is characterized by two oscillatory responses, one at the anti-resonance frequency of the cable and the other at the first anti-resonance frequency of the stator winding. The results show that the coils close to the neutral point are most stressed, in contrast with the state-of-art literature, which claims maximum voltage stress at the line end coil. The voltage stress across the coils close to the neutral point occurs due to voltage oscillations at the first anti-resonance frequency, which is a sole characteristic of the stator winding. Thus, the stator winding remains under stress even with short or no cable. Also, the CM PWM harmonics with a frequency close to the 1st anti-resonance frequency of the winding inevitably induces severe oscillations. In addition, the magnitude of the voltage stress depends on the common-mode impedance of the stator winding at the anti-resonance frequency, switching frequency, modulation index and the phase angle of the voltage space vector. Furthermore, it is advised to have a short cable length such that the first anti-resonance frequency of the cable is not close to the first anti-resonance frequency of the stator winding, otherwise, the voltage stress across the groundwall insulation may exceed the safety level.

The finding has a number of implications. First, the existing filtering techniques and standards aimed at limiting dv/dt may not work well. Secondly, since the first anti-resonant frequency of machine windings is relatively low, an increase in PWM frequency is more likely to excite the resonance. Hence more effective measure to suppress the oscillation at the machine anti-resonance needs to be developed in order to exploit the fast switching capability of WBG devices.

Appendix

A. Stator Slot Dimension: Stator inner diameter = 26.4 cm, Stator outer diameter = 16.19 cm, Stator stack length = 5.08 cm, Slot depth = 3.09 cm, Slot opening at air gap = 0.188 cm.

B. Stator Winding Parameters: No. of stator slots = 48, Stator turns per coil = 11, Parallel circuits per phase = 0, Coils in series per phase = 8, No. of wires in parallel = 12, Wire size = 20 AWG, Phase resistance = 0.77Ω.

C. Stator Winding Insulation Parameter: Turn insulation thickness = 0.105 mm, Turn insulation permittivity = 3.5 F/m, Main-wall insulation permittivity = 3.5 F/m, Ground-wall insulation thickness = 0.35 mm, Ground-wall insulation permittivity = 3.5 F/m.

D. Shielded Cable Parameters: No. of conductors = 4, Conductor cross-sectional area = 2.5 mm^2, No. of strands = 40, Strand size = 30, Core insulation thickness = 0.9 mm, Core insulation permittivity = 2.8 F/m, Jacket insulation thickness = 1.9 mm, Jacket insulation permittivity = 4 F/m.

REFERENCES

[1] A. M. F. El-Refaie and R. D. King, "Low-inductance, high efficiency induction machine and method of making same," U.S. Patent 2012 0 126 741 A1, May 24, 2012.

[2] D. Gerada, A. Mebarki, N. L. Brown, C. Gerada, A. Cavagnino, and A. Boglietti, "High-speed electrical machines: Technologies, trends, and developments," *IEEE Trans. Ind. Electron.*, vol. 61, no. 6, pp. 2946–2959, Jun. 2014.

[3] Y. Zhang, Q. Li, and D. Jiang, "A motor CM impedance based transformerless active EMI filter for DC-side common-mode EMI suppression in motor drive system", *IEEE Trans. Power Electron.*, vol. 35, no. 10, pp. 10238-10248, Oct. 2020.

[4] B. Bai, Y. Wang, and X. Wang, "Suppression for discharging bearing current in variable-frequency motors based on electromagnetic Shielding slot wedge", *IEEE Trans. Magn.*, vol. 51, no. 11, pp. 1-4, Nov. 2015.

[5] F. Dalvand, S. Dalvand, F. Sharafi, and M. Pecht, "Current noise cancellation for bearing fault diagnosis using time shifting", *IEEE Trans. Ind. Electron.*, vol. 64, no. 10, pp. 8138-8147, Oct. 2017.

[6] B. Mirafzal, G. L. Skibinski, and R. M. Tallam, "A failure mode for PWM inverter-fed AC motors due to the antiresonance phenomenon," *IEEE Trans. Ind. Appl.*, vol. 45, no. 5, pp. 1697-1705, Sept.-oct. 2009.

[7] R. E. Adjaye and K. J. Cornick, "Distribution of switching surges in the line-end coils of cable-connected motors," *IEE Journal Electric Power Appl.*, vol. 2, no. 1, pp. 11-21, February 1979.

[8] C. Petrarca, A. Maffucci, V. Tucci, and M. Vitelli, "Analysis of the voltage distribution in a motor stator winding subjected to steep-fronted surge voltages by means of a multiconductor lossy transmission line model," *IEEE Trans. Energy Convers.*, vol. 19, no. 1, pp. 7-17, March 2004.

[9] M. T. Wright, S. J. Yang, and K. McLeay, "General theory of fast-fronted interturn voltage distribution in electrical machine windings", *IEE Proc.*, vol.130, Pt. B, no. 4, pp. 245-256, July 1983.

[10] P. G. McLaren and H. Oraee, "Multiconductor transmission-line model for the line-end coil of large AC machines," *IEE Proc. Electric Power Appl.*, vol. 132, no. 5, pp. 278-, September 1985.

[11] L. Gubbala, A. von Jouanne, P. N. Enjeti, C. Singh, and H. A. Toliyat, "Voltage distribution in the windings of an AC motor subjected to high dv/dt PWM voltages", in *Proc. IEEE Power Electronics Specialist Conf. (PESC)*, pp.579-585, 1995.

[12] G. Suresh, A. Toliyat, A. Rendusara, and N. Enjeti, "Predicting the transient effects of PWM voltage waveform on the stator windings of random wound induction motors," *IEEE Trans. Power Electron.*, vol. 14, no. 1, pp. 23–30, Jan. 1999.

[13] M. K. Hussain and P. Gomez, "Modeling of machine coils under fast front excitation using a non-uniform multiconductor transmission line approach", in *Proc. IEEE North American Power Symposium (NAPS)*, Denver, CO, 2016.

[14] O. Magdun, S. Blatt, and A. Binder, "Calculation of stator winding parameters to predict the voltage distributions in inverter fed AC machines" in *Proc. IEEE Int. Symposium Diagnostics Electric Mach., Power Electron. and Drives (SDEMPED)*, pp. 447-453, Valencia, 2013.

[15] S. Sundeep, J. Wang, and A. Griffo, "Prediction of transient voltage distribution in inverter-fed stator winding, considering mutual couplings in time domain", in *Proc. IEEE Energy Conversion Congress & Expo. (ECCE),* Detroit, MI, USA, 2020.

[16] Y. Xie, J. Zhang, F. Leonardi, A. R. Munoz, M. W. Degner, and F. Liang, "Modeling and verification of electrical stress in inverter-driven electric machine windings," *IEEE Trans. Ind. Appl.*, vol. 55, no. 6, pp. 5818-5829, Nov.-Dec. 2019.

[17] Y. Xie, J. Zhang, F. Leonardi, A. R. Munoz, M. W. Degner, and F. Liang, "Voltage stress modeling and measurement for random-wound machine windings driven by inverters", *IEEE Trans. Ind. Appl.*, vol. 56, no. 4, pp. 3536-3548, July-Aug. 2020.

[18] J. L. Guardado, J. A. Flores, V. Venegas, J. L. Naredo, and F. A. Uribe, "A machine winding model for switching transient studies using network synthesis," *IEEE Trans. Energy Convers.*, vol. 20, no. 2, pp. 322-328, June 2005.

[19] J. J. Grainger and W. D. Stevenson Jr., *Power System Anlysis*, 1st ed., Singapore: Mc Graw Hill, Inc. 1994.

[20] H. De Paula, D. A. d. Andrade, M. L. R. Chaves, J. L. Domingos, and M. A. A. de Freitas, "Methodology for cable modeling and simulation for high-frequency phenomena studies in PWM motor drives," *IEEE Trans. Power Electron.*, vol. 23, pp. 744-752, Mar. 2008.

[21] D. Han, S. Li, Y. Wu, W. Choi, and B. Sarlioglu, "Comparative analysis on conducted CM EMI emission of motor drives: WBG versus Si devices," *IEEE Trans. Ind. Electron.*, vol. 64, no. 10, pp. 8353-8363, Oct. 2017.

[22] Mitch Olszewski (2011 Mar.). Evaluation of the 2010 toyota prius hybrid synergy drive system. Oak Ridge National Laboratory, USA. [Online] Available:https://info.ornl.gov/sites/publications/files/Pub26762.pdf.

BIOGRAPHIES

Shubham Sundeep received the B.Tech. degree in electrical engineering from National Institute of Technology Surat, India in 2015 and the M.Tech. degree in power electronics, electrical machines and drives from Indian Institute of Technology Delhi in 2017. He is currently pursing Ph.D degree in the Department of Electronics and Electrical Engineering, The University of Sheffield, Sheffield, UK. His research interests include Condition Monitoring, Diagnostics, Prognostics, and control of electrical machines, and electrical machine drives. Between 2017 and 2018, he was working as R&D Engineer in EATON Corporation where he worked on the control of synchronous drives.

Jiabin Wang (SM'03) received the B.Eng. and M.Eng. degrees from Jiangsu University, Zhengjiang, China, in 1982 and 1986, respectively, and the Ph.D. degree from the University of East London, London, U.K., in 1996, all in electrical and electronic engineering.

Currently, he is a Professor in Electrical Engineering at the University of Sheffield, Sheffield, U.K. From 1986 to 1991, he was with the Department of Electrical Engineering at Jiangsu University, where he was appointed a Lecturer in 1987 and an Associated Professor in 1990. He was a Postdoctoral Research Associate at the University of Sheffield, Sheffield, U.K., from 1996 to 1997, and a Senior Lecturer at the University of East London from 1998 to 2001. His research interests range from motion control and electromechanical energy conversion to electric drives for applications in automotive, renewable energy, household appliances and aerospace sectors. He is a fellow of the IET and a senior member of IEEE

Antonio Griffo (M'13) received the M.Sc. degree in electronic engineering and the Ph.D. degree in electrical engineering from the University of Napoli "Federico II," Naples, Italy, in 2003 and 2007, respectively. From 2007 to 2013, he was a Research Associate with the University of Sheffield, Sheffield, U.K., and the University of Bristol, Bristol, U.K. He is currently a Senior Lecturer with the Department of Electronic and Electrical Engineering, University of Sheffield. His research interests include modeling, control, and condition monitoring of electric power systems, power electronics converters, and electrical motor drives for renewable energy, automotive, and aerospace applications.

Fernando Alvarez-Gonzalez received the B.Eng. degree in electronic engineering and M.Eng. degree in electrical and electronic engineering from the University of Oviedo, Asturias, Spain in 2012 and 2014 respectively. He received the Ph.D. degree in electronic and electrical engineering at The University of Sheffield, Sheffield, U.K in 2019. From 2018 he has been a postdoctoral research associate at The University of Sheffield's EMD group. His current research interests include modelling, fault detection and condition monitoring of permanent magnet synchronous machines.